University of Reading

Sensitivity of simulated mesoscale convective systems over East Asia to the treatment of convection in a high-resolution GCM

Article

Published Version

Creative Commons: Attribution 4.0 (CC-BY)

Open access

Li, P. ORCID: https://orcid.org/0000-0002-4812-2184, Muetzelfeldt, M. ORCID: https://orcid.org/0000-0002-6851-7351, Schiemann, R. ORCID: https://orcid.org/0000-0003-3095-9856, Chen, H., Li, J., Furtado, K. and Zhuang, M. (2023) Sensitivity of simulated mesoscale convective systems over East Asia to the treatment of convection in a high-resolution GCM. Climate Dynamics, 60. pp. 2783-2801. ISSN 0930-7575 doi: https://doi.org/10.1007/s00382-022-06471-2 Available at https://centaur.reading.ac.uk/107100/

It is advisable to refer to the publisher's version if you intend to cite from the work. See Guidance on citing.

To link to this article DOI: http://dx.doi.org/10.1007/s00382-022-06471-2

Publisher: Springer

All outputs in CentAUR are protected by Intellectual Property Rights law, including copyright law. Copyright and IPR is retained by the creators or other copyright holders. Terms and conditions for use of this material are defined in

the End User Agreement.

www.reading.ac.uk/centaur

CentAUR

Central Archive at the University of Reading

Reading's research outputs online

Climate Dynamics
https://doi.org/10.1007/s00382-022-06471-2

Sensitivity of simulated mesoscale convective systems over East Asia to the treatment of convection in a high-resolution GCM

Puxi Li[1,2] · Mark Muetzelfeldt[3] · Reinhard Schiemann[3] · Haoming Chen[1,2] · Jian Li[1,2] · Kalli Furtado[4] · Moran Zhuang[5]

Received: 11 March 2022 / Accepted: 15 August 2022
© The Author(s) 2022

Abstract
Mesoscale convective systems (MCSs) downstream of the Tibetan Plateau (TP) exhibit unique precipitation features. These MCSs can have damaging impacts and there is a critical need for improving the representation of MCSs in numerical models. However, most global climate models are typically run at resolutions that are too coarse to reasonably resolve MCSs, and it is still unclear how well higher-resolution global models can reproduce the precipitation characteristics of MCSs. In this study, the sensitivity of MCSs simulated by a global high resolution (~ 10 km), atmosphere-only climate model to different treatments of convection (with and without parametrized convection, and a hybrid representation of convection) have been investigated. The results show that explicit convection (i.e., non-parameterized) can better reproduce the observed pattern of MCS precipitation over the East Asian Summer Monsoon region. In general, explicit convection better simulates the diurnal variability of MCSs over the eastern China, and is able to represent the distinctive diurnal variations of MCS precipitation over complex terrain particularly well, such as the eastern TP and the complex terrain of central-northern China. It is shown that explicit convection is better at simulating the timing of initiation and subsequent propagating features of the MCS, resulting in better diurnal variations and further a better spatial pattern of summer mean MCS precipitation. All three experiments simulate MCS rainfall areas which are notably smaller than those in observations, but with much stronger rainfall intensities, implying that these biases in simulated MCS morphological characteristics are not sensitive to the different treatment of convection.

Keywords Mesoscale convective systems · Precipitation characteristics · Convection parameterization · Diurnal variations · East Asia · Complex terrain

1 Introduction

Mesoscale convective systems (MCSs) are organized collections of precipitating cumulonimbus clouds and generally persist for several hours (Houze 2004, 2018). They play a vital role in regulating the hydrological and energy cycle, modulating the atmospheric circulation at both regional and global scales (Yuan and Houze 2010; Feng et al. 2016, 2021; Schumacher and Rasmussen 2020). MCSs can generate extreme rainfall and induce flash floods, severe winds, and even downbursts aligned with the intense deep convection (Zipser et al. 2006; Houze 2018; Song et al. 2019, 2021). Because of these damaging impacts, MCSs can cause heavy casualties and property losses.

The summer MCSs downstream of the Tibetan Plateau (TP) exhibit unique precipitation features due to the rugged underlying surface and a complex interplay with the

✉ Haoming Chen
chenhm@cma.gov.cn

1 State Key Laboratory of Severe Weather, Chinese Academy of Meteorological Sciences, China Meteorological Administration, Beijing 100081, China

2 Research Center for Disastrous Weather Over Hengduan Mountains and Low-Latitude Plateau, China Meteorological Administration, Kunming 650034, China

3 National Centre for Atmospheric Science, Department of Meteorology, University of Reading, Reading, UK

4 Met Office, Exeter, UK

5 LASG, Institute of Atmospheric Physics, Chinese Academy of Sciences, Beijing 100029, China

Published online: 01 September 2022

large-scale monsoon circulations (Cui et al. 2020; Yang et al. 2020; Zhang et al. 2018), and long-lived MCSs are responsible for a majority of heavy precipitation and further cause catastrophic floods over the EASM (Chen et al. 2014, 2017; Guan et al. 2020). There is a critical need for improving the representation of MCSs in numerical models, in order to alleviate their damaging impacts (Prein et al. 2017a, b; Chen and Kirtman 2018; Feng et al. 2018). State-of-the-art global models cannot adequately resolve MCSs, owing to the insufficient model horizontal resolution (Bukovsky and Karoly 2011; Kooperman et al. 2014). Some important processes of MCSs and other forms of the deep convection, such as the triggering, entrainment and detrainment of the convective elements, are not explicitly resolved with the typical horizontal resolution of current global models and must be parameterized (Prein et al. 2015). Representing multi-scale interaction of different processes in MCSs, acting from convective to synoptic scale, is a fundamental issue in developing these parameterizations (Yang et al. 2017; Schumacher and Rasmussen 2020). More field campaigns are needed to elucidate these interconnections and for a better process understanding, that the convection parameterization can be based on (Houze 2018). Therefore, representing MCS dynamics properly in a parameterized way still remains a need and a challenge in traditional global models.

With the rapid development of computing resources, convection-permitting models (CPMs) with finer grid-spacing (typically ≤ 5 km) make it possible to resolve important aspects of deep convection in an explicit way and remove the reliance upon convection parameterization. This approach has been gradually applied to climate modelling in order to provide more reliable climate information (Prein et al. 2015, 2017c; Guo et al. 2019, 2020; Stevens et al. 2019, 2020). Improvements of CPMs in simulating precipitation have been found in terms of the diurnal variations over subtropical land regions (Li et al. 2020a; Ou et al. 2020), and precipitation intensity-frequency structure (Zhang and Chen 2016; Ban et al. 2021) and the MCSs (Prein et al. 2017a; Yun et al. 2020; Guo et al. 2022), although the amount of precipitation is generally overestimated in the CPMs (Prein et al. 2015; Li et al. 2020a; Yun et al. 2020).

Prein et al. (2017a) found that their CPM can capture the general characteristics of an MCS over the east of the U.S., as well as its propagating features. Feng et al. (2018) used the Weather Research and Forecasting (WRF) model at convection-permitting scales (WRF-CPM) to compare different cloud microphysics schemes (Morrison and Thompson) in simulating MCSs over the central U.S. They found that more simulated stratiform precipitation of the MCS in the Thompson microphysics parameterization can favor a relatively longer duration, through a stronger dynamical feedback to the larger-scale environments. Yun et al. (2020) investigated the performance of a WRF-CPM (~ 3 km) over southern China in simulating the MCS properties, and they found that the WRF-CPM can successfully reproduce the spatial pattern and seasonal march of MCS geneses and occurrences, but also demonstrated that the WRF-CPM overestimates the MCS occurrence and activities, which results in an overestimation of the contribution from MCSs to total precipitation. Guo et al. (2022) evaluated a WRF-CPM (~ 4 km) over eastern China based on an object-based algorithm, and found that the WRF-CPM can well capture the duration and the propagation direction of precipitation systems, but the coverage area of the simulated systems are significantly larger with weak precipitation intensities.

Although the aforementioned analyses have discussed the performance of regional CPM in simulating precipitation characteristics of MCSs over the central U.S., as well as eastern China, it is still unclear how faithfully a global high-resolution model at grid spacing of O(10 km) represents a climatology of MCS properties over the EASM domain, downstream of the TP. In addition, although it is considered that a model can reasonably resolve some important aspects of deep convection at horizontal resolutions of finer than 4 km (Prein et al. 2015), some studies have documented that models using explicit convection exhibit some improvements in simulating convection and precipitation at horizontal grid spacing much coarser than 4 km and thus across the intermediate 'grey zone' of deep convection. For instance, Ou et al. (2020) demonstrated that WRF with explicit convection better simulates the diurnal variations of precipitation over the TP at a horizontal resolution of 9 km, compared to three simulations with different convection parameterization. Pearson et al. (2014) found that the diurnal cycle of precipitation over West Africa is better captured when the Met Office Unified Model uses explicit convection, even at 12 km resolution. Marsham et al. (2013) found that the more realistic explicit convection in the Met Office Unified Model simulation at 12 km resolution could have upscale effects on the larger scale circulations and further results in a better representation of the West African low-level monsoonal flow. Vergara-Temprado et al. (2020) further revealed that models with explicit convection can have benefits at much coarser resolution (≤ 25 km) than previously considered, for example bringing improvements in simulating the diurnal variations and frequency-intensity structure of precipitation, particularly over the flat areas of their European domain. Since the typical horizontal scale of organized MCS is hundreds of kilometers, it is of interest to ask the question: what is the difference between an explicit or a parameterized representation of convection at O(10 km) in simulating the overall precipitation characteristics of MCSs?

The aim of the present work is to investigate the sensitivity of simulated MCSs to the different treatment of convection (fully parameterized convection, fully explicit convection and hybrid convection) in a high-resolution GCM

(~ 10 km) over the EASM, through applying a novel iterative rain cell tracking method to identify and track intense MCSs in high-resolution satellite observations and three different configurations of high-resolution global Met Office Unified Model simulations.

The remainder of the article is organized as follows. Section 2 describes observation datasets, analysis methods, the experimental design and the model simulation we have used. Section 3 presents the main results, including the differences among three model configurations in simulating the summer mean MCS precipitation, as well as the precipitation characteristics of MCSs over the EASM, including the diurnal variations, duration, rainfall area and average/ maximum hourly precipitation. Finally, a brief summary and a discussion are given in Sect. 4.

2 Data and methodology

2.1 Experimental design

By using global simulations instead of regional simulations, we perform our modelling without lateral boundary conditions, and the associated spin-up of convective features. This allows us to potentially capture phenomena such as mid-latitude and tropical interactions with the EASM in a physically consistent way across scales. Our simulations are fully described in Muetzelfeldt et al. (2021), here we note the important aspects for this study. We make use of free running high-resolution global Met Office Unified Model simulations performed with three different configurations: fully parametrized convection (N1280-PC), fully explicit convection (N1280-EC) and hybrid convection (N1280-HC). The configuration for N1280-PC was HadGEM3-GC3.1 (Williams et al. 2018), using a 4-min time step to allow it to be run at higher resolution. The boundary conditions, for e.g., sea surface temperature and sea ice, were broadly based on the HighResMIP protocol (Haarsma et al. 2016), although the GLOMAP-mode aerosol (Mulcahy et al. 2018) scheme was used instead of MACv2-SP aerosols (Stevens et al. 2017). N1280-PC uses the standard Unified Model convection parametrization scheme (Williams et al. 2018).

N1280-EC has all convection parametrization schemes disabled; hence all moist convection is modelled by the model's internal dynamics and cloud physics schemes. N1280-HC has the deep convection scheme disabled but retains the same shallow and mid-level convection schemes as in N1280-PC. There are some minor differences between the different simulations, which are fully described in Muetzelfeldt et al. (2021) and summarized here. The differences between N1280-PC and N1280-EC are partly necessitated by disabling the convection parametrization scheme; the stochastic kinetic energy backscatter and stochastic perturbed tendencies schemes depend on the convection parametrization scheme being enabled and so are also disabled in N1280-EC. Additionally, in N1280-EC, horizontal diffusion is enabled, and a 3-min time step is used, both for reasons of numerical stability, and a prognostic representation of graupel is used. The only other minor difference, apart from the difference in convection schemes, between N1280-HC and N1280-PC is that N1280-HC uses a higher value of 5800 s (instead of 3600 s) for the convective available potential energy closure timescale, as this has been shown to improve the representation of African easterly waves (Tomassini 2018). All three simulations were run for at least 4 years covering the period 2005–2008.

2.2 Observation dataset

We used the Climate Prediction Center's morphing technique (CMORPH; Joyce et al. 2004) satellite-retrieved precipitation product. This product covers the period studied here, from 2005 to 2008, with a horizontal grid spacing of approximately 8 km and a temporal resolution of 30 min. In this study, we convert the original 30 min temporal resolution product into an hourly precipitation product, and mainly focus on the MCS precipitation over East Asia in boreal summer (June-July–August). To enhance the comparison between the CMORPH satellite retrievals and the three HadGEM3-GC3.1 simulation, we convert the CMORPH product onto the model grid by using the areal conservative remapping method in NCAR Command Language (https://www.ncl.ucar.edu/Document/Functions/Built-in/area_conserve_remap.shtml), then apply the iterative raincell tracking method and conduct follow-up analysis.

In terms of revealing the spatial distributions of total precipitation over East Asia, the Global Precipitation Climatology Project, 1 degree daily precipitation product (GPCP-1DD, with a horizontal grid spacing of $1° \times 1°$ and a daily temporal resolution; Huffman et al. 2001) and Tropical Rainfall Measuring Mission (TRMM) 3B42 V7 rainfall product (TRMM-3B42, with a horizontal grid spacing of $0.25° \times 0.25°$ and a 3-hourly temporal resolution; Huffman et al. 2007) have also been used.

2.3 Iterative raincell tracking method

We use the precipitation variable to identify intense MCSs in the CMORPH observations and simulations. The MCS tracking approaches used in this study are similar to the previous studies, such as Davis et al. (2009), Clark et al. (2014) and Prein et al. (2017a, b). These approaches align well with the MCS definition proposed by Houze (2004), which identified a MCS as continuous precipitation areas (having a typical diameter longer than 100 km in at least one direction) that live for a few hours.

In this study, we identify and track intense MCSs in space and time by using an "iterative raincell tracking (IRT)" technique (Moseley et al. 2013, 2019; Li et al. 2020b). For each time step independently, connected areas with surface precipitation exceeding a predetermined threshold are recognized as objects in the first step. The weighted center, rainfall area, and mean/max surface precipitation intensity within the rainfall area are all recorded for each labelled object. An MCS is defined as a single entity with intense precipitation (≥ 3.0 mm h^{-1}) covering an area larger than 3600 km^2 and lasting at least two hours. This threshold is set to exclude too small and non-MCS storms, thus allows us to track intense storms with relatively enough size, which follows the same threshold settings in the previous study of Li et al. (2020b). Additional sensitivity tests using 5.0 mm h^{-1} and 2.5 mm h^{-1} have demonstrated that while the changing thresholds will impact the amount of discovered MCS, the overall MCS features remain robust and do not change the conclusions revealed in this study. Here we focus on the sensitivity of different treatment of deep convection in simulating intense MCSs because of their high socio-economic importance.

The method looks for overlaps between each object with objects from the previous and subsequent time steps and saves the object IDs associated with those overlaps. In terms of handling of merging and fragmentation incidents: if an object overlaps with more than one object in a previous or subsequent time step, only the two biggest objects are recorded; the other objects are disregarded. A convergent iterative algorithm repeats the object identification numerous times to account for the fact that objects move over time, more details of the convergent iterative algorithm can be found in Moseley et al. (2019) and Li et al. (2020b). Each succeeding iteration step estimates the object's advection velocity and incorporates it into the future iteration's detection procedure. Finally, overlapping objects are integrated into a single track.

In addition, based on the different underlying surface types, diurnal features and MCS precipitation characteristics, four specific sub-regions over eastern China are defined in study, the same as those mentioned in the previous studies (Li et al. 2020a, b), which are the eastern periphery of the Tibetan Plateau (ETP; 27.0°N–34.0°N, 102.5°E–110.5°E), the middle-to-lower reaches of the Yangtze River Basin (YRB-ML; 27.0°N–33.0°N, 110.5°E–121.5°E), southeastern China (SEC; 21.0°N–27.0°N, 102.5°E–117.5°E) and the lower reaches of the Yellow River Basin (LYB; 33.0°N–38.0°N, 110.5°E–120.0°E). These are shown in Fig. 4.

3 Results

3.1 Performance in simulating total EASM precipitation

We first investigate the performance of different configurations of HadGEM3-GC3.1 at the O(10 km) grid spacing in simulating the summer mean precipitation over the EASM region (Fig. 1). In general, all three observational datasets (i.e., CMORPH, TRMM and GPCP) agree well with each other regarding the spatial distribution of summer mean precipitation (Fig. 1a–c): TRMM and GPCP have relatively high pattern correlation coefficients (PCC) of 0.91 and 0.89, and have a low root-mean-square errors (RMSE) of 1.04 mm day^{-1} and 1.16 mm day^{-1}, compared to the CMORPH, respectively. There are three rainfall centers over the EASM region (the summer rainfall located in South China Sea is neglected in this study): one is located over southeastern China, the second rain-belt is named as the "Mei-yu" (in China) and "Chang-ma" (in South Korea), and the third one is called the "Bai-u" (in Japan) which is located in southern Japan.

The three HadGEM3-GC3.1 simulations generally agree with the CMORPH, but there are also some deficiencies in each simulation: N1280-EC can well reproduce the spatial distributions of the observed precipitation (with a PCC of 0.66 and a RMSE of 2.96 mm day^{-1}), but it overestimates precipitation over southeastern China and underestimates the "Mei-yu" and "Chang-ma" rain-belt, as well as underestimating the precipitation over southern Japan (Fig. 1d). Both N1280-HC (hybrid version) and N1280-PC (fully-parameterized version) overestimate the precipitation over southern China and underestimate the precipitation within the "Mei-yu" and "Chang-ma" rain-belt (with a relatively lower PCC of 0.54 and 0.60, and a higher RMSE of 3.42 and 3.30 mm day^{-1}, compared with the N1280-EC), but better represent the magnitude of precipitation over southern Japan (Fig. 1e, f).

3.2 Sensitivity to different treatment of convection in simulating MCS precipitation

3.2.1 Summer MCS tracks and the spatial distribution of summer mean MCS precipitation

We further check the sensitivity to different treatment of convection (explicit vs. hybrid vs. fully-parametrized) in simulating MCS precipitation at the O(10 km) grid spacing. The number of summer mesoscale convective system (MCS) within each $1° \times 1°$ grid box among observations and simulation during the study period from 2005 to 2008

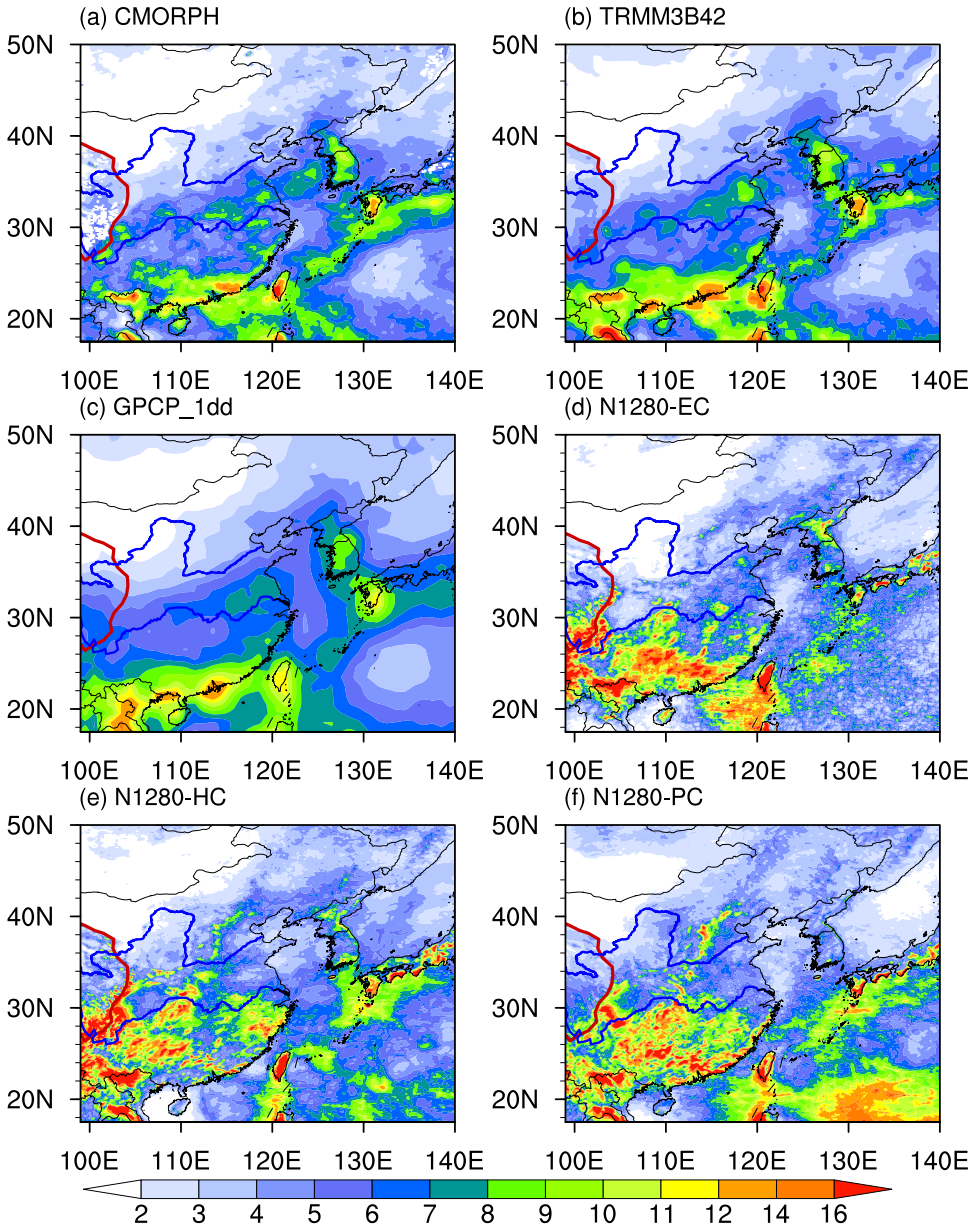

Fig. 1 Spatial distributions of summer total precipitation from 2005 to 2008 in observation and simulation: **a** CMORPH, **b** TRMM 3B42, **c** GPCP_1dd, **d** N1280-EC, **e** N1280-HC, and **f** N1280-PC. Here blue lines indicate the Yellow River and Yangtze River, respectively, and the red contour indicates the TP where the topography exceeds 2700 m

are shown in Fig. 2. A total of 3370, 3493, 2499 and 2630 intense MCS precipitation systems over the EASM region were tracked in CMORPH, N1280-EC, N1280-HC and N1280-PC, respectively. It should be noted that the density map of MCSs in the N1280-EC simulation (Fig. 2b) has a good resemblance with CMORPH, but has slightly more MCSs than observed (+3.6%). The overestimated MCSs mostly located over southeastern China, while the MCSs were slightly underestimated within the "Mei-yu" and "Changma" rain-belt in N1280-EC. Both the N1280-HC (Fig. 2c) and the N1280-PC (Fig. 2d) have fewer MCSs over the coastal regions in southeastern China and adjacent sea areas, as well as within the "Mei-yu" and "Changma" rain-belt. As a result, the N1280-HC (− 25.8%) and the N1280-PC (− 22.0%) have considerably fewer MCSs compared with those observed in CMORPH (Fig. 2a).

The spatial distributions of MCS precipitation among observations and simulation are shown in Fig. 3. There are three main MCS precipitation centers over the EASM region, in accordance with the summer total precipitation: one rainfall center is located over southeastern China, one center is the southwest-northeast-elongated rain belt, which is called "Mei-yu" in China and "Chang-ma" in South Korea, and the third one is located in southern Japan (Fig. 3a). The MCSs contribute up to 55.0% of the total precipitation over the abovementioned areas (Fig. 3e), which indicates that the MCSs play an essential role in modulating the water cycle over the East Asia.

Table 1 The number of MCS tracks over the East Asian Summer Monsoon (EASM) region, as well as the minimum and maximum duration of the MCS among the CMORPH, N1280-EC, N1280-HC and N1280-PC simulation

	The number of MCS tracks over the EASM region	The minimum and maximum of MCS duration among OBS and simulation (unit: h)	
		Min	Max
CMORPH	3370	2	117
N1280-EC	3493	2	97
N1280-HC	2499	2	159
N1280-PC	2630	2	86

N1280-HC and N1280-PC fail to properly reproduce the spatial distributions of the summer MCS precipitation over the EASM domain (Fig. 3c, d), with a relatively lower PCC of 0.65 and 0.61, and a higher RMSE of 1.45 mm day^{-1} and 1.48 mm day^{-1}, respectively. Specifically, they cannot simulate the precipitation over southeastern China (Fig. 3c, d), and underestimate the summer MCS precipitation within the "Mei-yu" and "Chang-ma" rain-belt (Fig. 3c, d). As a result, the contribution of MCS to total precipitation is also considerably less in these two simulations, particularly over southeastern China (Fig. 3g, h). However, they better simulate the MCS precipitation over southern Japan (Fig. 3c, d). Another interesting feature is that the MCS precipitation in the N1280-HC and N1280-PC is anchored by the topography along the so-called "second-step" to "third-step" terrain region (the region where the 300, 600, 900 m topography contours become denser around 32°–40 N°) over eastern China (Fig. 3c, d), which indicates that the precipitation enhancement effects of the topography are magnified in these two model configurations; this will be specifically discussed in the later Sect. 3.2.2. The overestimation of precipitation along the steep terrain region is smaller in N1280-HC (Fig. 3c), compared with those in N1280-PC (Fig. 3d).

Among three different model configurations, N1280-EC best reproduces the observed pattern of MCS precipitation (Fig. 3b), with a higher PCC of 0.72 and a lower RMSE of 1.37 mm day^{-1}, compared with N1280-HC and N1280-PC. It well simulates the MCS precipitation center over southeastern China and better reproduces the "Mei-yu" and "Chang-ma" rain-belt (Fig. 3b), as well as having a good resemblance with CMORPH in terms of the contribution of MCS to total precipitation over southeastern China and the "Mei-yu" and "Chang-ma" rain-belt (Fig. 3f). However, N1280-EC still has some obvious deficiencies: it overestimates the MCS precipitation over southeastern China but

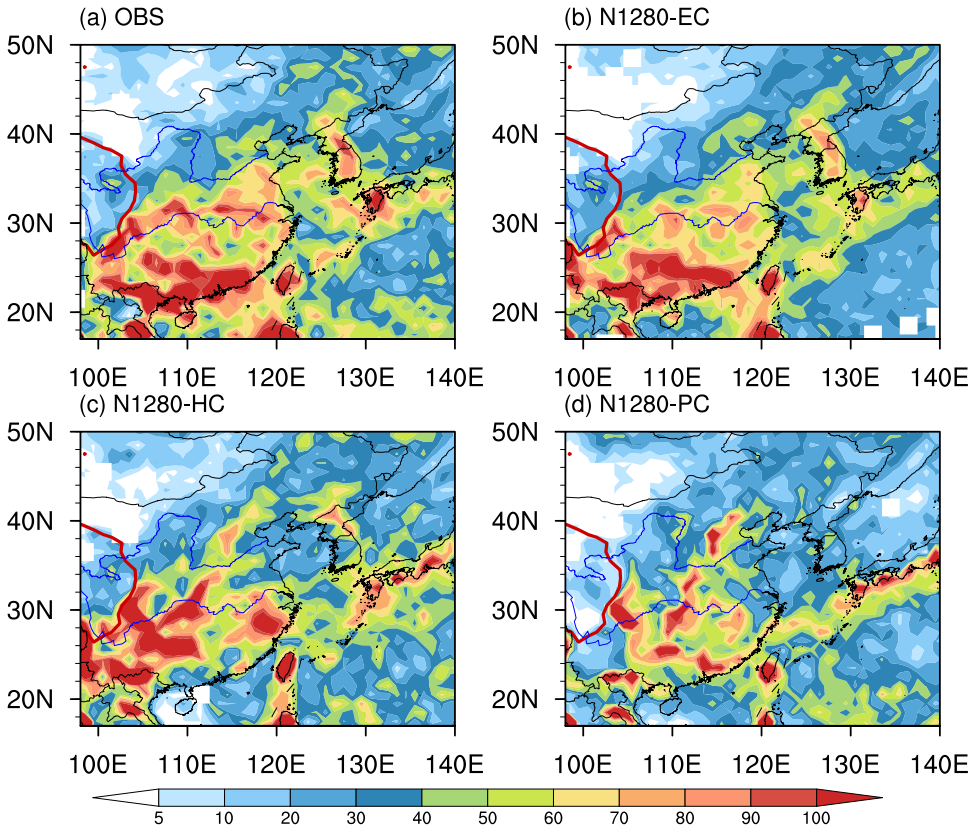

Fig. 2 The number of summer mesoscale convective systems (MCSs) within each 1°×1° grid box during the study period from 2005 to 2008 among observation and simulation: **a** CMORPH, **b** N1280-EC, **c** N1280-HC, and **d** N1280-PC. Here blue lines indicate the Yellow River and Yangtze River, respectively, and the red contour indicates the TP where the topography exceeds 2700 m

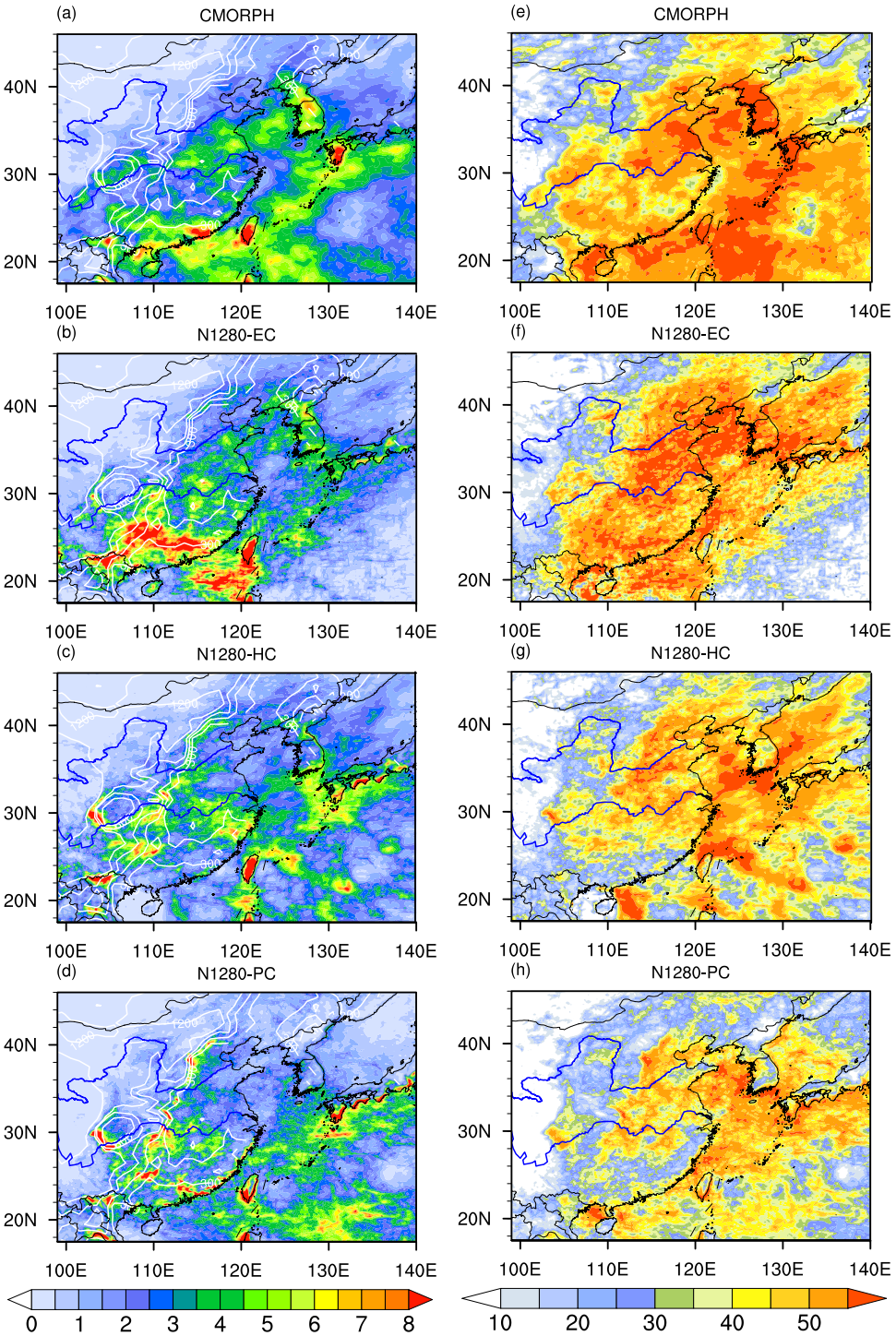

Fig. 3 Spatial distributions of MCS precipitation (**a**–**d**; unit: mm day^{-1}) from 2005 to 2008 and MCS contribution to total precipitation (**e**–**h**; unit: %) in observation and simulation: (**a**, **d**) CMORPH, (**b**, **f**) N1280-EC, (**c**, **g**) N1280-HC, and (**d**, **h**) N1280-PC. Here blue lines indicate the Yellow River and Yangtze River, respectively. The white contours in **a**–**d** represent surface elevation (unit: m), where 300, 600, 900, 1200, 2700 m contours are drawn

underestimates the magnitude of "Mei-yu" and "Chang-ma" rain-belt, as well as the MCS precipitation over southern Japan (Fig. 3b).

3.2.2 The diurnal cycle of MCS precipitation

The diurnal cycle of convective precipitation exhibits some interesting behavior over the EASM region, such as a phase delay running east–west along the Yangtze River (Yu et al. 2007, 2014; Chen et al. 2010). As such, the diurnal cycle represents a rigorous test-bed for validating convection parametrizations and other physical schemes in numerical models (Dai 2006; Yuan et al. 2013; Zhou et al. 2018; Li et al. 2020a). In this study, one of the most remarkable differences among the three model configurations is the different diurnal variations of the MCS

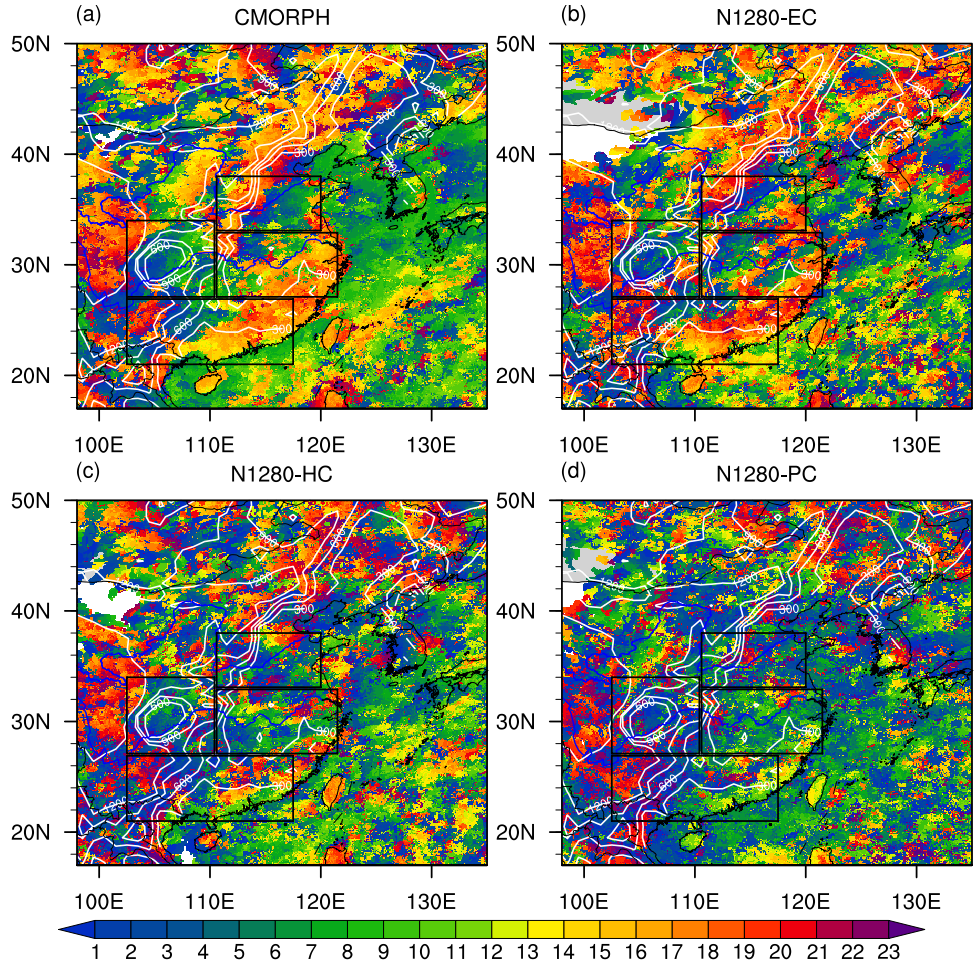

Fig. 4 Spatial distributions of the local solar time (hereafter "LST" in short; colored) of the maximum in the composite diurnal cycle of the summer MCS precipitation frequency over the East Asia among observations and simulations: **a** CMORPH, **b** N1280-EC, **c** N1280-HC and **d** N1280-PC. Here the middle-left rectangle indicates the eastern periphery of the Tibetan Plateau, the middle-right rectangle indicates the middle-to-lower reaches of the Yangtze River Basin, the bottom rectangle indicates southeastern China and the top-right rectangle indicates the lower reaches of the Yellow River Basin. The white contours represent surface elevation (unit: m), where 300, 600, 900, 1200, 2700 m contours are drawn

precipitation over the EASM region (Figs. 4, 5). In observations, the diurnal variations of MCS precipitation over the eastern periphery of the Tibetan Plateau (ETP) are dominated by the nocturnal precipitation (Figs. 4a, 5a), which is due to the low-level moisture transport increasing after sunset and reaching its maximum before dawn, similar to the diurnal variations of the total precipitation which have been documented in previous studies (Chen et al. 2010; Chen et al. 2014; Zhang et al. 2018; Muetzelfeldt et al. 2021). It should be noted that there is a marked regional difference over this steep terrain region. To the west of the ETP, it is the late-afternoon precipitation that dominates the diurnal variations at higher altitudes (regions where the topography exceeds 2700 m) over the TP (Fig. 4a), which is quite different from the nocturnal/morning peak at lower altitudes (i.e., the Sichuan Basin) within the ETP region (Li et al. 2021a, b).

All HadGEM3-GC3.1 simulations well simulate the nighttime MCS precipitation over the ETP (Fig. 4b–d), although with a stronger magnitude (Fig. 5a). However, N1280-PC cannot reproduce the late-afternoon MCS precipitation at higher altitude regions over the TP: it produces more nocturnal rainfall at higher altitudes over the TP than the observed, and therefore incorrectly reproduces the distinct regional features of the diurnal variations over this complex terrain region (Fig. 4d). In contrast, N1280-EC and N1280-HC better reproduce the late-afternoon MCS precipitation at higher altitudes over the TP.

In CMORPH, the diurnal variations of MCS precipitation in the monsoonal "Mei-yu" and "Chang-ma" rain-belt are dominated by the early morning diurnal peaks (Fig. 4a), because of the early-morning acceleration of the low-level monsoon flow and the subsequent strengthening of its convergence (Chen et al. 2013, 2017; Guan et al. 2020). The MCS precipitation in the middle-to-lower reaches of the Yangtze River basin (YRB-ML) in eastern China exhibits two diurnal peaks: one is the early-morning peak; the other one is the late-afternoon rainfall peak (Figs. 4a, 5b), which is associated with more "surface-driven" intense MCS precipitation that occurs beyond the large-scale monsoonal rain-belt and become predominantly active during the "break" monsoon periods, based on previous studies (Yuan and Houze 2010; Yu et al. 2014; Yu and Li 2015). The MCS precipitation over the southeastern China (SEC) shows

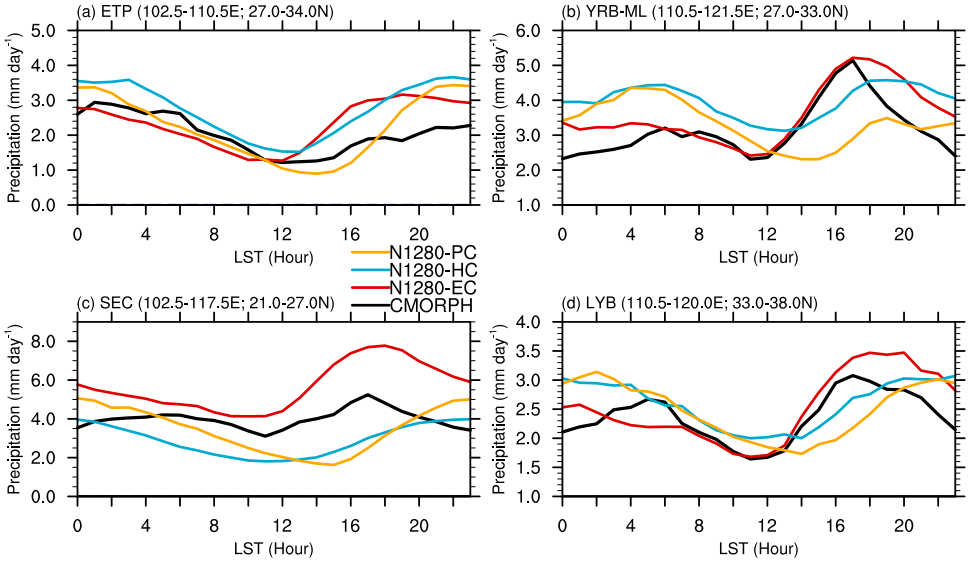

Fig. 5 Diurnal variations of summer mean MCS precipitation averaged over different sub-regions in Eastern China: **a** the eastern periphery of the Tibetan Plateau (ETP; 27.0°N–34.0°N, 102.5°E–110.5°E); **b** the middle-to-lower reaches of the Yangtze River Basin (YRB-ML; 27.0°N–33.0°N, 110.5°E–121.5°E), **c** southeastern China (SEC; 21.0°N–27.0°N, 102.5°E–117.5°E) and **d** the lower reaches of the Yellow River Basin (LYB; 33.0°N–38.0°N, 110.5°E–120.0°E) among observations and model simulations (unit: mm day^{-1}). Here the black, red, blue and oranges lines indicate the observation, N1280-EC, N1280-HC and N1280-PC simulation, respectively

two weak diurnal peaks in observations (Figs. 4a, 5c): one primary peak during late-afternoon (1600–1800 LST) and a weak secondary peak in the nighttime to early-morning (0200–0800 LST). The MCS precipitation over the lower reaches of the Yellow River basin (LYB) exhibits two comparable diurnal peaks (Figs. 4a, 5d).

In the simulations, N1280-HC and N1280-PC both overestimate the magnitude of nighttime MCS precipitation over the YRB-ML (Fig. 5b) and LYB (Fig. 5d). A consistent model bias of N1280-HC and N1280-PC (especially N1280-PC) is that there is a 3–5 h delayed phase in simulating the late-afternoon MCS precipitation peak over mainland eastern China (observed at 1600–1800LST), including the YRB-ML, the SEC, as well as the LYB (Fig. 5b–d). In addition, N1280-HC and N1280-PC cannot simulate the diurnal variations of the MCS precipitation over the central north China. Specifically, both N1280-HC and N1280-PC (Fig. 4c, d) cannot reproduce the northwest-to-southeast delayed phase from mountain to plain along around the 40 N° (Fig. 4a), which will be discussed in more detail in Sect. 3.2.3.

In contrast, N1280-EC better simulates the diurnal variations of MCS precipitation over the YRB-ML (Fig. 5b), SEC (Fig. 5c), as well as LYB (Fig. 5d), particularly for the phase of the peaks. Furthermore, N1280-EC reproduces the diurnal variations of the MCS precipitation over central north China (Fig. 4a, b), which indicates that the explicit convection version can reproduce the initiation as well as the propagating features of the MCSs, which generally form over the mountain regions in the afternoon, then propagate downstream at night, inducing heavy rainfall.

The results here are consistent with and complementary to those of Muetzelfeldt et al. (2021), who analysed the same simulations and found that the summertime diurnal cycle of total precipitation over Asia was best simulated in model configurations without parameterized convection. Furthermore, they found that the diurnal variations only improved at finer resolution in simulations without parameterized convection. Here, we have looked at a dynamical phenomenon, and so our results show that the general findings of Muetzelfeldt et al. (2021) apply to specific features, MCSs, over Asia. This could be interpreted in two ways—these are not necessarily mutually exclusive. First, the improved diurnal cycle at large (synoptic) scales leads to a corresponding improvement in the diurnal cycle at smaller scales, including that of MCSs. Second, the improved representation of MCSs, as shown above in Sect. 3.2.1 showing the number of simulated MCSs, leads to an upscale improvement in the diurnal cycle. In our view, the first of these is most likely, although further work would be required to disentangle these two effects (Table 1).

3.2.3 Properties of observed and simulated MCSs over the EASM

After evaluating the model differences in simulating the diurnal variations of the MCS precipitation, the MCS statistical properties, including MCS lifetime, rainfall area, average/ maximum hourly precipitation over four sub-regions among CMORPH and simulation are shown in Fig. 6. In general, all three different configurations agree well with the CMORPH in terms of the MCS duration (Fig. 6a), but the MCS in the N1280-HC simulation has relatively longer duration, compared with other two configurations and CMORPH (Fig. 6a).

The most distinct differences between CMORPH and the HadGEM3-GC3.1 simulations are in the rainfall area (Fig. 6b) and intensity (Fig. 6c, d) of the MCSs. The MCSs in the all the three different configurations of HadGEM3-GC3.1 simulations have a notably smaller rainfall area (Fig. 6b), but with a much stronger rainfall intensity (both the average and maximum hourly precipitation; Fig. 6c, d), compared with CMORPH. This indicates that the model behaviors relating to the spatial morphological characteristics (such as the rainfall area and intensity) of MCS precipitation systems might not be sensitive to the different treatment of convection, and should be attributed to other key elements or parameterizations in the model, for instance the evolution of density currents in the boundary-layer parameterization as in Jucker et al. (2020).

We proceed to investigate the performance of the three model configurations in simulating the dynamical evolution of long-lived MCS precipitation characteristics (MCS rainfall area: Fig. 7; maximum hourly precipitation: Fig. 8) over eastern China from a statistical standpoint. It should be noted that the solid line in Figs. 7 and 8 indicate the mean of MCSs to represent the general features of the dynamic evolution of MCS precipitation properties, and the shadings indicates the interquartile range across all MCSs.

In general, the three different configurations can partly reproduce the dynamical evolution of the MCS rainfall area, but with a systematic underestimation during almost the whole lifetime, among all four sub-regions (Fig. 7a–d). The MCS rainfall area in the HadGEM3-GC3.1 simulations increases more slowly in the developing stage and does not grow to a large-enough size at mature stage, compared with that in CMORPH (Fig. 7). Over the YRB-ML, the MCS rainfall area in all three HadGEM3-GC3.1 simulations persists for longer than in CMORPH (Fig. 7b), consistent with the longer MCS duration over the YRB-ML in the simulation (Fig. 6a). Among all three model configurations, the MCS rainfall area in N1280-HC persists relatively longer over ETP (Fig. 7a), YRB-ML (Fig. 7b), as well as LYB (Fig. 7d), compared with those in the CMORPH and other two configurations.

There exists an obvious asymmetry in the dynamical evolution of the MCS maximum hourly precipitation (Fig. 8). The MCS rainfall intensity increases quickly, reaching its peak intensity during the developing stage (Fig. 8). This kind of intense convective precipitation is related to the strong updrafts within an MCS when the precipitating cumulonimbus clouds aggregate and develop.

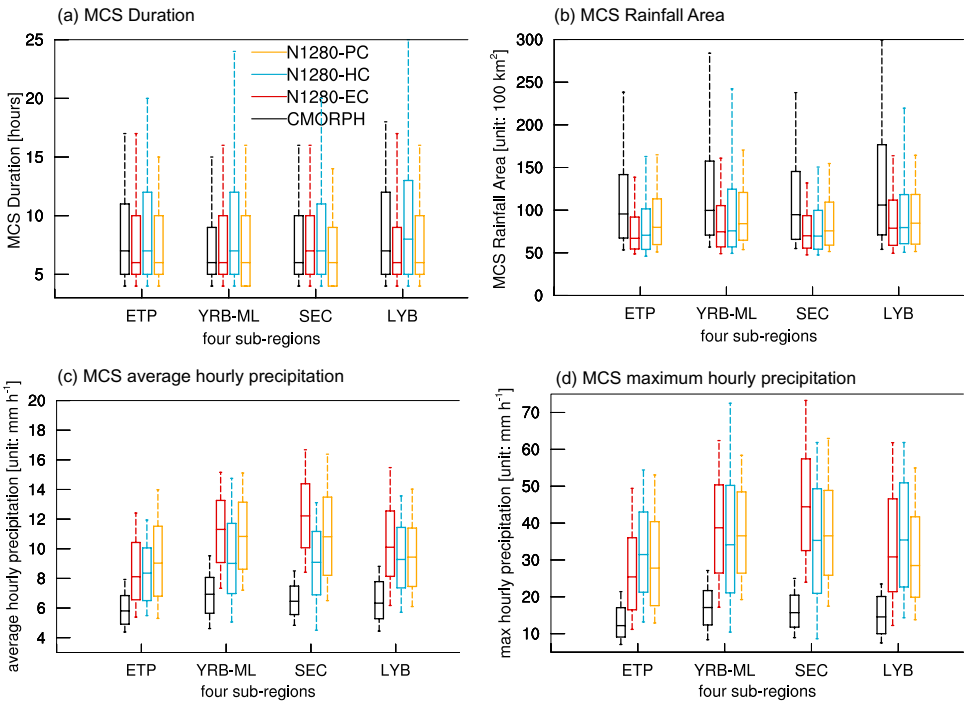

Fig. 6 Overall MCS statistical characteristics over four sub-regions among observations and model simulations: **a** MCS duration (unit: h), **b** MCS rainfall area (unit: 10^2 km^2), **c** MCS average hourly precipitation (unit: mm h^{-1}), **d** MCS maximum hourly precipitation (unit: mm h^{-1}). Here the black, red, blue and oranges lines indicate CMORPH, N1280-EC, N1280-HC and N1280-PC, respectively. In the boxplot, the horizontal bars denote the medium values, the boxes indicate the interquartile range (25% and 75%), and the whiskers represent 10% and 90% percentile values

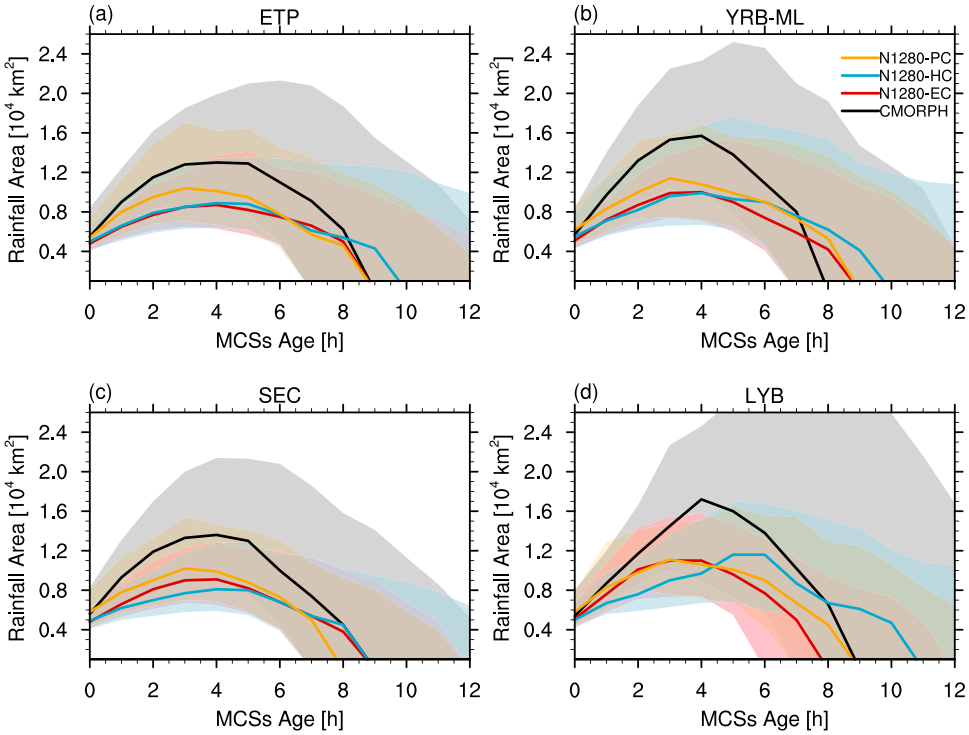

Fig. 7 Development of long-lived (duration ≥ 6 h) MCS rainfall area as a function of MCS age in CMORPH (black) and model simulation (red: N1280-EC; blue: N1280-HC; orange: N1280-PC) over four sub-regions: **a** ETP, **b** YRB-ML, **c** SEC, and **d** LYB. Here the shadings/error bars show the interquartile spread in each sample, the solid line shows the medium values. The *x*-axis indicates the MCS age (unit: h), the *y*-axis indicates MCS rainfall area (unit: 10^4 km^2)

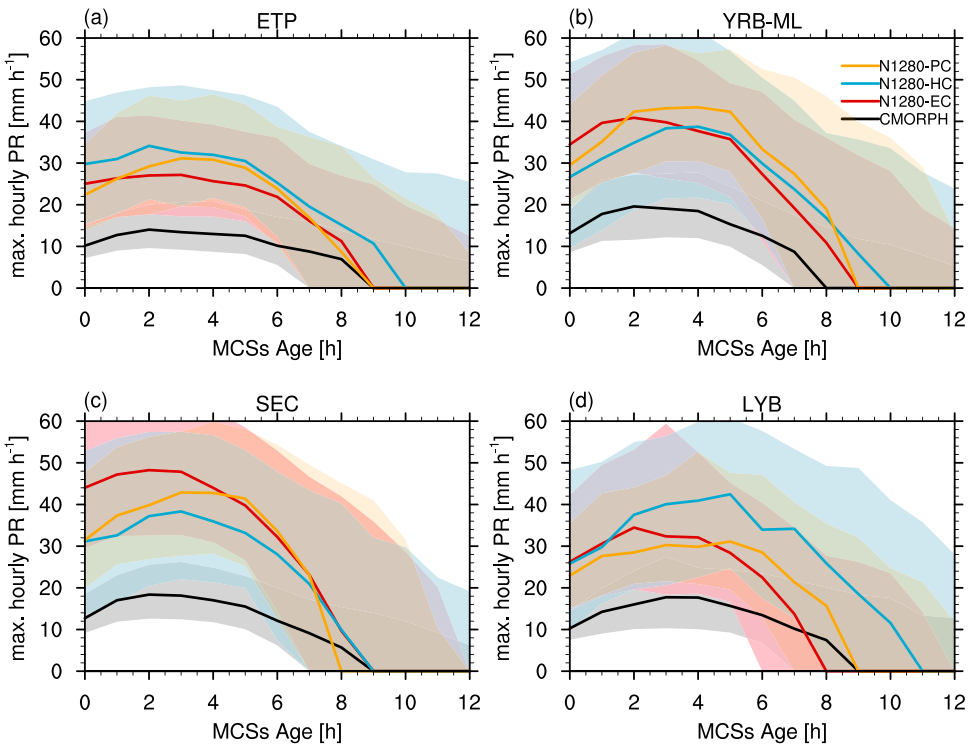

Fig. 8 Same as Fig. 7, but for the development of MCS maximum hourly precipitation as a function of MCS age (unit: mm h^{-1})

Then the MCS rainfall intensity gradually weakens with a slower rate for the remainder of the MCS's lifetime (Fig. 8). This kind of relatively moderate stratiform precipitation is induced by large-scale condensation when the updrafts become weaker and cannot support vertical advection of precipitation particles, as mentioned in previous studies (Houze 2004, 2018). All three model configurations of the HadGEM3-GC3.1 can generally reproduce the asymmetry in the development of MCS rainfall

intensity, but the maximum hourly precipitation intensity in the simulations is about three times higher than in CMORPH.

3.2.4 Different model behaviors in simulating summer MCS precipitation over complex terrain

There is a distinct difference among the three configurations in simulating summer MCS precipitation over complex terrain. Here this difference is illustrated for a region in central north China, and the underlying physical mechanisms are investigated.

The spatial distributions of summer MCS precipitation over central north China, as well as their diurnal variations are shown in Figs. 9 and 10. A consistent model bias in N1280-PC is that the excessive MCS precipitation is anchored by steep terrain: too much MCS precipitation is concentrated at the mountain slope (the areas where the topography is between the 300 m and 600 m; Fig. 9d), associated with the low-level convergence on the windward slope of the mountain. Additionally, the magnitude of the

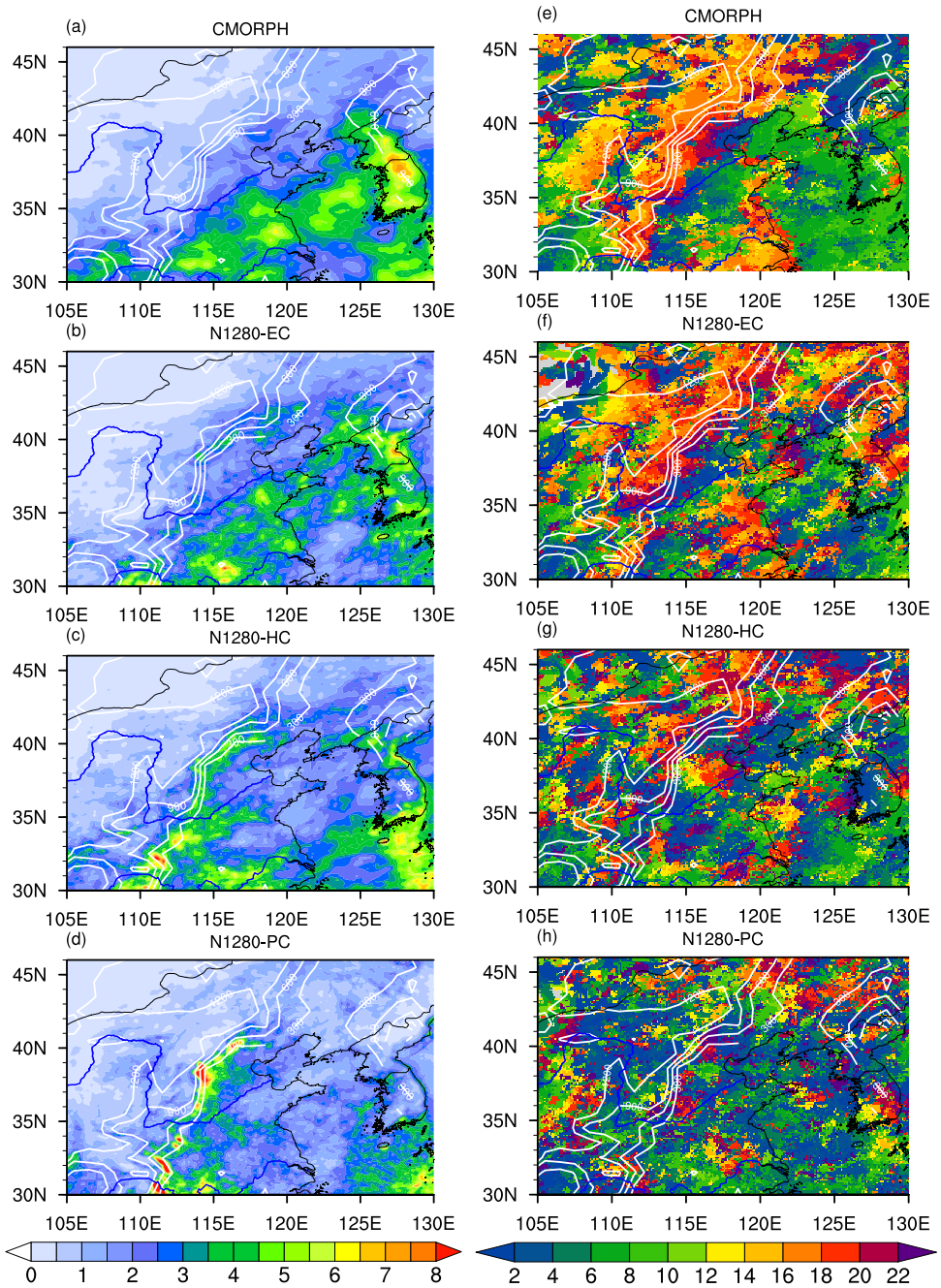

Fig. 9 Spatial distributions of summer MCS precipitation (unit: mm day^{-1}) and the maximum phase in the diurnal variations of the summer MCS precipitation frequency over the central north China and its surrounding regions: **a** CMORPH, **b** N1280-EC, **c** N1280-HC, and **d** N1280-PC. The white contours represent surface elevation (unit: m), where 300, 600, 900, 1200 m contours are drawn. The blue lines indicate the Yellow River and Yangtze River, respectively

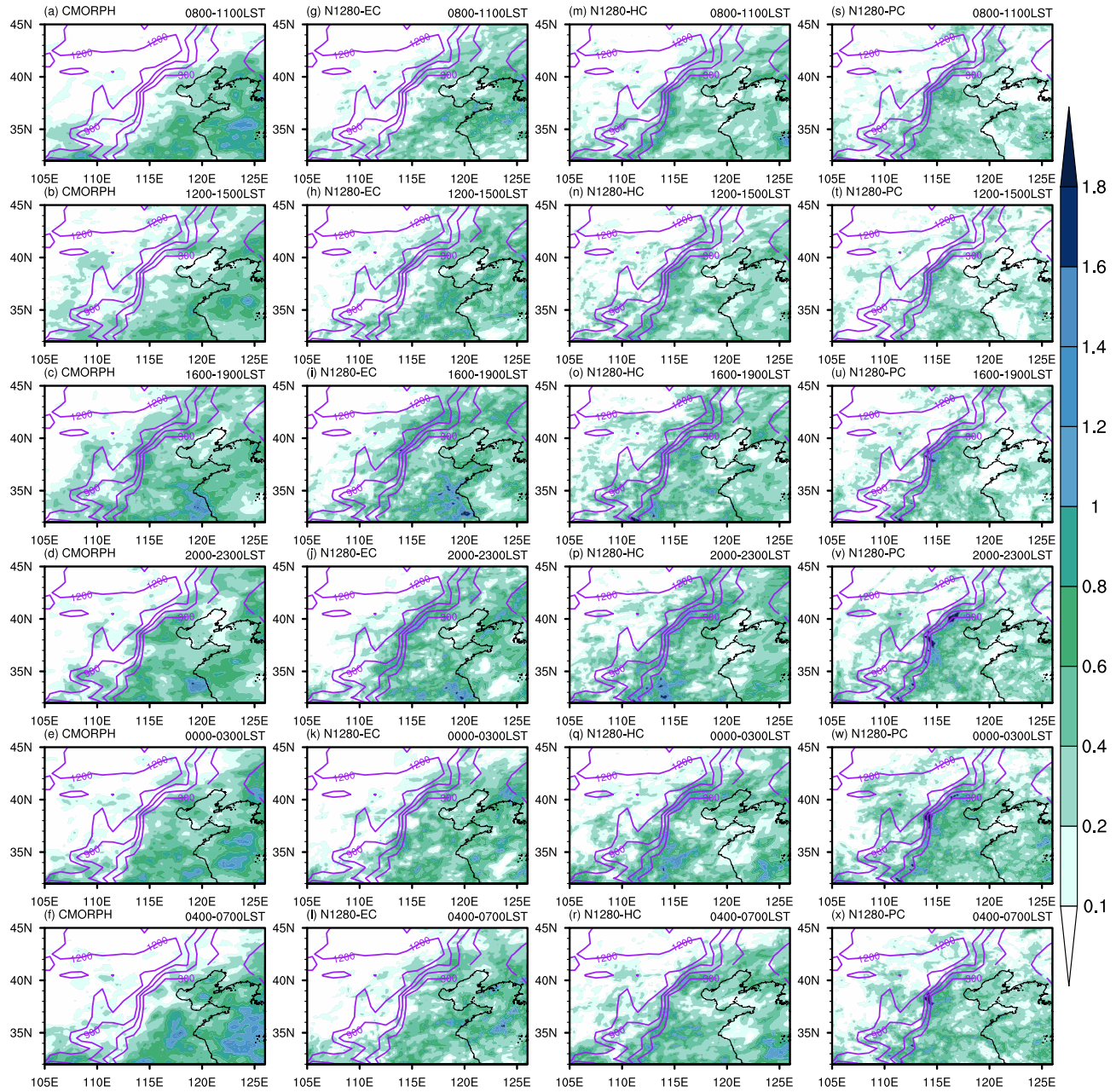

Fig. 10 Diurnal variations of every 4-h (0800-1100LST, 1200-1500LST, 1600-1900LST, 2000-2300LST, 0000-0300LST and 0400-0700LST) accumulated summer precipitation (unit: mm day^{-1}) over the central north China and its surrounding regions among **a–f** CMORPH, **g–l** N1280-EC, **m–r** N1280-HC and **s–x** N1280-PC. The purple contours represent surface elevation (unit: m), where 300, 600, 900, 1200 m contours are drawn

"Mei-yu" and "Chang-ma" rain-belt is significantly underestimated in N1280-PC, especially the MCS precipitation over the lower-to-middle reaches of the Yangtze River basin in China, as well as the MCS precipitation over South Korea. Therefore, N1280-PC has relatively lower skill over in simulating the spatial pattern of the MCS precipitation over central north China and its surroundings, with a low PCC value of 0.41 and a high RMSE value of 1.59 mm day^{-1} (Fig. 9d). The overestimation of the summer MCS precipitation along steep terrain is partly reduced in N1280-HC (Fig. 9c), which might indicate a benefit from using a hybrid convection scheme, but similar kinds of model bias were also found in this model configuration. Thus N1280-HC has moderate skill in simulating the MCS precipitation pattern, with a PCC value of 0.57 and a RMSE value of 1.33 mm day^{-1}.

A step-change improvement was found between N1280-HC to N1280-EC (from Fig. 9b–c), when the convection parametrization scheme is completely disabled. The

excessive MCS precipitation over the steep terrain region has been mostly eliminated, and the "Mei-yu" and "Changma" rain-belt are much better depicted (Fig. 9b). As a result, the N1280-EC has higher skill in reproducing the spatial distributions of the MCS precipitation, with a higher PCC value of 0.76 and a lower RMSE value of 0.98 mm day^{-1}.

We further investigated the diurnal variations and propagating features of the summer MCS precipitation over central north China in CMORPH observations and three simulations (Figs. 10, 11, 12). In CMORPH, the MCS precipitation initializes and enhances over the northwestern mountainous region in the late-afternoon (Figs. 10c, 12a), thereafter the organized convection propagates to the lower altitudes, i.e., the southeastern plains (Figs. 10d, e; 12a). The diurnal variations of MCS precipitation are related to the MCS propagating features, as shown by the averaged moving direction and speed of MCSs in Fig. 11. The observed MCSs move eastward from northwestern mountainous region to the southeastern plain with velocities of 35–40 km h^{-1} (Fig. 11a), resulting in intriguingly pronounced spatial distributions of the MCS diurnal variations associated with the topography, where an obvious delayed phase can be seen from northwestern mountains to southeastern plains (Figs. 9e, 12a). Following sunrise, the MCS precipitation over the mountains rapidly decreases (Fig. 10f), and reaches a minimum around local noon (Figs. 10a, 12a).

N1280-PC cannot accurately reproduce the late-afternoon MCS precipitation over the northwestern mountain (Figs. 10u, 12d), nor can it simulate the propagating features of the MCS precipitation (Figs. 10v; 12d). In contrast, too much MCS precipitation is seen at lower altitudes following the steep terrain (Figs. 10u, 12d), whereas too little MCS precipitation is seen over the northwestern mountainous region where it should occur (Fig. 10c). The excessive MCS precipitation center at lower altitudes in the steep terrain persists throughout the night (Figs. 10v–x, 12d), and continues to exist even after sunrise (Figs. 10s, t, 12d). These phenomena are also reflected in the averaged MCS propagation direction and speed (Fig. 11). In N1280-PC, there are much more MCSs at lower altitudes alongside the steep terrain, and the MCSs remain quasi-stationary with a much lower propagation speed (Fig. 11d), compared to those in CMORPH observations (Fig. 11a). Therefore, the summer MCS precipitation in N1280-PC exhibits inaccurate diurnal variations (Figs. 9h, 12d) and distinct wet biases related to the complex terrain over central north China (Fig. 9d).

In N1280-HC, the excessive night MCS precipitation at lower altitudes along the steep terrain is not as pronounced as that in N1280-PC (Figs. 10o–r, 12c), but the MCS in N1280-HC still preferentially occurs and exhibits a quasi-stationary propagating feature at lower altitudes along the steep terrain (Fig. 11c), and the summer MCS precipitation remains active throughout the day (Fig. 10m–r), thus leading to a similar wet bias of the summer MCS precipitation in N1280-HC (Fig. 9c).

In contrast to N1280-PC and N1280-HC, N1280-EC can better reproduce the late-afternoon MCS precipitation over mountainous region (Figs. 10h, i, 12b), as well as represent

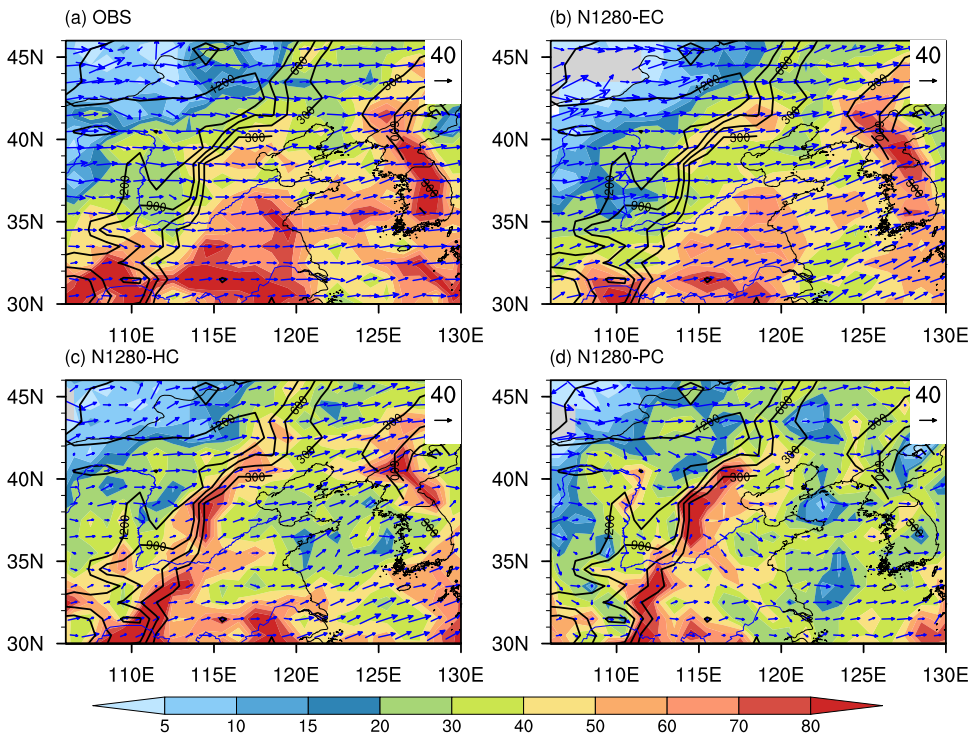

Fig. 11 The averaged MCS propagation direction and speed (vectors; unit: km h^{-1}), and the number of summer MCSs (shadings) within each 1° × 1° grid box during the study period over the central north China and its surrounding regions among **a** CMORPH, **b** N1280-EC, **c** N1280-HC and **d** N1280-PC. Here the black contours represent surface elevation (unit: m), where 300, 600, 900, 1200 m contours are drawn

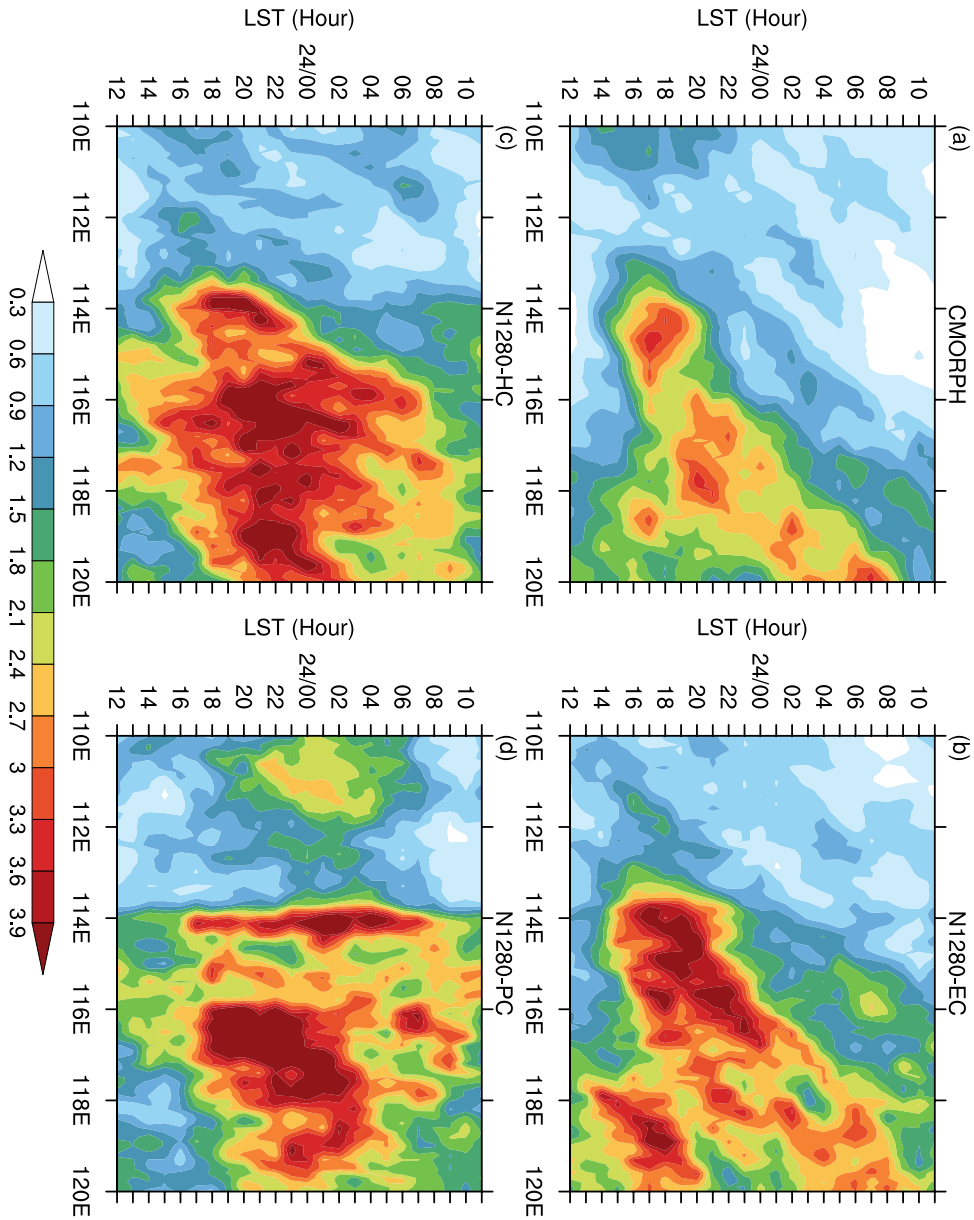

Fig. 12 Time-longitude Hovmöller diagram (Local Solar Time versus 0.1° Longitude bin) of hourly MCS rainfall diurnal variations (unit: mm day^{-1}) among **a** CMORPH, **b** N1280-EC, **c** N1280-HC and **d** N1280-PC over central north China (time-longitude cross section for the 37° N–42° N zone). Here the *x*-axis indicates longitude (unit: °E), the *y*-axis indicates the local solar time (unit: h)

the propagating features of the organized convection systems from late-afternoon to night (Figs. 10j, k, 12b). In addition, N1280-EC reasonably simulates the direction and speed of the summer MCS propagating features (Figs. 11b, 12d), and better depicts the underlying diurnal variations of MCS precipitation over central north China (Figs. 9f, 10g–l). As a result, N1280-EC better simulates the spatial distribution of the summer MCS precipitation over this complex terrain region (Fig. 9b) and closely resembles CMORPH (Fig. 9a).

4 Summary and discussion

4.1 Summary

In this study, we have used an iterative rain cell tracking method to identify and track intense MCSs in CMORPH observations and three model configurations of HadGEM3-GC3.1 (fully-explicit convection: N1280-EC,

hybrid convection: N1280-HC and fully-parametrized convection: N1280-PC) at the O(10 km) grid spacing. We have investigated the sensitivity of simulated MCS precipitation over East Asia to the treatment of convection in this model, the major findings are summarized as below.

It is found that N1280-HC and N1280-PC have considerably fewer MCS tracks over the coastal regions in southeastern China and adjacent sea areas, as well as within the "Mei-yu" and "Chang-ma" rain-belt, resulting in an underestimation of − 25.8% and − 22.0% over the East Asia, compared with those in CMORPH. The density map of MCSs in the N1280-EC simulation has a good resemblance with CMORPH, with a slight overestimation of + 3.6%.

There are three main MCS precipitation centers over the EASM, which are not well represented in N1280-PC and N1280-HC simulations. For instance, they cannot simulate the precipitation over southeastern China, and underestimate the MCS precipitation within the "Mei-yu" and "Chang-ma" rain-belt. N1280-HC and N1280-PC have relatively lower PCCs of 0.65 and 0.61 compared with CMORPH, and higher RMSEs of 1.45 mm day^{-1} and 1.48 mm day^{-1}, respectively. In contrast, N1280-EC can better reproduce the observed pattern of MCS precipitation. It is better at simulating the MCS precipitation center over the southeastern China, and better at reproducing the "Mei-yu" and "Chang-ma" rain-belt, and thus has a higher PCC of 0.72 and a lower RMSE of 1.37 mm day^{-1} compared with the other two model configurations. Hence, N1280-EC is demonstrably better at representing the geographical distributions of MCS precipitation over the EASM, although it overestimates the MCS precipitation over southeastern China.

One of the most remarkable differences among three model configurations is the different diurnal variations of the MCS precipitation. In general, N1280-HC and N1280-PC both overestimate the magnitude of nighttime MCS precipitation over the YRB-ML and LYB. A consistent model bias of these two versions (especially N1280-PC) is that they have a 3–5 h delayed phase in simulating late-afternoon MCS precipitation peak over mainland eastern China. In comparison, N1280-EC better simulates the diurnal variations of MCS precipitation over the YRB-ML, SEC and LYB. We also found that N1280-EC can better represent the distinct diurnal variations over complex terrain, such as the regions surrounding the eastern periphery of the Tibetan Plateau (higher mountains versus lower valleys), as well as over the complex terrain of central north China. This indicates that N1280-EC is better at reproducing the timing of initiation and subsequent propagation of the MCS precipitation, resulting in a better diurnal variations.

The difference in simulating diurnal variations is also reflected in the spatial distributions of summer mean MCS precipitation over regions with complex terrain. A detailed investigation focusing on central north China showed that the diurnal variations of MCS precipitation are related to the MCS propagating features in CMORPH. The observed MCSs initialize and enhance over the northwestern mountains in the late-afternoon and then propagate to the southeastern plain downstream with velocities of 35.0–40.0 km h^{-1}, resulting in a pronounced delayed phase from northwestern mountains to southeastern plains in the diurnal variations over central north China. In contrast, excessive MCS precipitation in N1280-PC is anchored to the low altitudes alongside steep terrain, and too much MCS precipitation is concentrated in the areas between the 300 m and 600 m contours, which mainly result from the incorrect diurnal variations induced by the deep convection scheme. This leads to a lower skill in simulating the spatial distributions of the summer MCS precipitation over central north China. N1280-HC has moderate skill, and a step-change improvement was found in N1280-EC. In this model, appropriate propagating features and realistic diurnal variations result in a more accurate simulation of the geographical distributions of summer mean MCS precipitation over the complex terrain in central north China.

The MCS statistical precipitation properties have been also investigated. All three simulations agree well with the CMORPH regarding the MCS duration. An interesting aspect is that the simulated MCSs in all three simulations have a notably smaller rainfall area but a much stronger rainfall intensity (both the average and maximum hourly precipitation) than those seen in CMORPH. This result indicates that the model behaviors on the morphological characteristics (such as rainfall area and precipitation intensity) of MCS is not sensitive to the different treatment of convection in these simulations. There should be some other key elements or parameterizations that result in these biases, for instance, the evolution of density currents in the boundary-layer parameterization according to a previous study (Jucker et al. 2020), the number of prognostic moments in the cloud microphysics scheme, or the insufficient model horizontal resolution.

4.2 Discussion

MCSs are inherently a combination of cumulus and mesoscale dynamics, coupled to the underlying thermodynamic changes associated with the phase change of water, and capturing these interconnections poses challenges for convection parameterization schemes. Here we have shown that this is the case for the total number of simulated MCSs (Sect. 3.2.1) and the diurnal variations and propagation of MCS precipitation (Sect. 3.2.2) in a O(10 km) global climate model, which shows that there is still considerable room to further improve the cumulus scheme and other model physics. This is important and necessary, because it will be decades until the computing

and storage technology to increase sufficiently to allow climate models running at kilometer-scales. Representing MCSs or other kinds of deep convection in a more appropriate parametrized way has the potential to provide benefits immediately and could, for example, improve the hydrological cycle over regions such as East Asia.

Although the explicit convection configuration better simulates the timing of initiation and propagating features of MCS, resulting in a better diurnal variation and furthermore a better representation of summer mean MCS precipitation, there are still some notable biases in N1280-EC, such as the notably stronger precipitation intensities with smaller rainfall areas, which implies that a horizontal resolution of O(10 km) may not be sufficient to resolve all kinds of MCS, although previous literature have documented that the numerical models permit convection at much coarse horizontal resolutions than previous considered and can have some benefits in simulating some aspects of precipitation characteristics (Hohenegger et al. 2020; Vergara-Temprado et al. 2020). Finer resolutions are still required, and other model physics should also be modified in accordance with the higher resolution, in order to achieve a more realistic simulation of MCSs in the near future. A series of studies have documented that the intense MCS have become more frequent and will be more violent in a warming world (Feng et al. 2016; Taylor et al. 2017; Prein et al. 2017b). The simulations investigated in this study are promising in this regard but currently have substantial mean-state biases in Asian precipitation, thus tuning of these simulations should be a priority (Muetzelfeldt et al. 2021).

The intense MCSs haven been identified and tracked by using precipitation variable in this work. For future studies, more atmospheric variables (including cloud-top brightness temperature, as well as radar reflectivity) can be jointly considered to give a more comprehensive description of MCS properties and its dynamical evolution over some specific regions, such as the eastern periphery of the TP. In addition, the relationship between the convection severity and precipitation intensity in different kinds of precipitating clouds deserves to be further investigated, so that the observational features can serve as metrics to thoroughly evaluate the performance of the CPM and other high resolution models.

Acknowledgements This work is jointly supported by the National Key R&D Program of China (2019YFC1510004 and 2021YFC3000904), the National Natural Science Foundation of China (42005039, 42075154, U2142214 and 42105026), and the Basic Research Fund of CAMS (2020Z006 and 2020Y009). Dr. Reinhard Schiemann, Dr. Mark Muetzelfeldt, and Dr. Kalli Furtado were funded by the COSMIC Project (P106301) and the UK-China Research & Innovation Partnership Fund through the Met Office Climate Science for Service Partnership (CSSP) China as part of the Newton Fund. This is a contribution no 11 to CORDEX-FPS-CPTP.

Author contributions All the authors made contributions to the conception and design of the research. PL did the analyses and drafted the work and others contributed to the revising and editing of the paper. HC and JL acquired the funding and supervised the research.

Funding This work is jointly supported by the National Key R&D Program of China (2019YFC1510004 and 2021YFC3000904), the National Natural Science Foundation of China (42005039, 42075154, U2142214 and 42105026), the Basic Research Fund of CAMS (2020Z006 and 2020Y009), the COSMIC Project (P106301) and the UK-China Research and Innovation Partnership Fund through the Met Office Climate Science for Service Partnership (CSSP) China as part of the Newton Fund. This is a contribution no 11 to CORDEX-FPS-CPTP.

Availability of data and materials The high-resolution global Met Office Unified Model (N1280) simulation output data are available upon request, as each simulation is over 80 TB in size and stored on the Met Office Managed Archive Storage System (MASS). CMORPH data are available from ftp://ftp.cpc.ncep.noaa.gov/precip/CMORPH_V1.0/CRT/8km-30min/. GPCP-1DD data are available from https://rda.ucar.edu/datasets/ds728.3/. TRMM 3B42 data are available from https://disc.gsfc.nasa.gov/datasets/TRMM_3B42_7/.

Code availability This study used NCL (NCAR Command Language) and CDO (Climate Data Operators) software. NCL is an open source interpreted language, designed specifcally for scientific data visualization and processing. CDO is a collection of many operators for standard processing of climate and forecast model data. Both are freely available at http://www.ncl.ucar.edu and http://www.mpimet.mpg.de/cdo, respectively.

Declarations

Conflict of interest The authors declare that they have no conflict of interest.

Open Access This article is licensed under a Creative Commons Attribution 4.0 International License, which permits use, sharing, adaptation, distribution and reproduction in any medium or format, as long as you give appropriate credit to the original author(s) and the source, provide a link to the Creative Commons licence, and indicate if changes were made. The images or other third party material in this article are included in the article's Creative Commons licence, unless indicated otherwise in a credit line to the material. If material is not included in the article's Creative Commons licence and your intended use is not permitted by statutory regulation or exceeds the permitted use, you will need to obtain permission directly from the copyright holder. To view a copy of this licence, visit http://creativecommons.org/licenses/by/4.0/.

References

Muetzelfeldt MR, Schiemann R, Turner AG, Klingaman NP, Vidale PL, Roberts MJ (2021) Evaluation of Asian summer precipitation in different configurations of a high-resolution GCM at a range of decision-relevant spatial scales. Hydrol Earth Syst Sci Discuss. https://doi.org/10.5194/hess-2020-652

Ban N, Caillaud C, Coppola E, Pichelli E, Sobolowski S, Adinolfi M, Ahrens B, Alias A, Anders I, Bastin S, Belušić D, Berthou S, Brisson E, Cardoso RM, Chan SC, Christensen OB, Fernández J, Fita L, Frisius T, Gašparac G, Giorgi F, Goergen K, Haugen JE, Hodnebrog Ø, Kartsios S, Katragkou E, Kendon EJ, Keuler K,

Lavin-Gullon A, Lenderink G, Leutwyler D, Lorenz T, Maraun D, Mercogliano P, Milovac J, Panitz H-J, Raffa M, Remedio AR, Schär C, Soares PMM, Srnec L, Steensen BM, Stocchi P, Tölle MH, Truhetz H, Vergara-Temprado J, de Vries H, Warrach-Sagi K, Wulfmeyer V, Zander MJ (2021) The first multi-model ensemble of regional climate simulations at kilometer-scale resolution, part I: evaluation of precipitation. Clim Dyn 57(1–2):275–302

Bukovsky MS, Karoly DJ (2011) A regional modeling study of climate change impacts on warm-season precipitation in the Central United States. J Clim 24(7):1985–2002

Chen G, Kirtman BP (2018) Long-lived mesoscale convective systems of superparameterized CAM and the response of CAM. J Adv Model Earth Syst 10(9):2269–2286

Chen H, Yu R, Li J, Yuan W, Zhou T (2010) Why nocturnal long-duration rainfall presents an eastward-delayed diurnal phase of rainfall down the Yangtze River valley. J Clim 23(4):905–917

Chen G, Sha W, Sawada M, Iwasaki T (2013) Influence of summer monsoon diurnal cycle on moisture transport and precipitation over eastern China. J Geophys Res Atmos 118(8):3163–3177

Chen G, Yoshida R, Sha W, Iwasaki T, Qin H (2014) Convective instability associated with the eastward-propagating rainfall episodes over Eastern China during the warm season. J Clim 27(6):2331–2339

Chen G, Sha W, Iwasaki T, Wen Z (2017) Diurnal cycle of a heavy rainfall corridor over East Asia. Mon Weather Rev 145(8):3365–3389

Clark AJ, Bullock RG, Jensen TL, Xue M, Kong F (2014) Application of object-based time-domain diagnostics for tracking precipitation systems in convection-allowing models. Weather Forecast 29(3):517–542

Cui W, Dong X, Xi B, Liu M (2020) Cloud and precipitation properties of MCSs along the Meiyu frontal zone in Central and Southern China and their associated large-scale environments. J Geophys Res Atmos 125(6):e2019JD031601

Dai A (2006) Precipitation characteristics in eighteen coupled climate models. J Clim 19(18):4605–4630

Davis CA, Brown BG, Bullock R, Halley-Gotway J (2009) The method for object-based diagnostic evaluation (MODE) applied to numerical forecasts from the 2005 NSSL/SPC spring program. Weather Forecast 24(5):1252–1267

Feng Z, Leung LR, Hagos S, Houze RA, Burleyson CD, Balaguru K (2016) More frequent intense and long-lived storms dominate the springtime trend in central US rainfall. Nat Commun 7:13429

Feng Z, Leung LR, Houze RA, Hagos S, Hardin J, Yang Q, Han B, Fan J (2018) Structure and evolution of mesoscale convective systems: sensitivity to cloud microphysics in convection-permitting simulations over the United States. J Adv Model Earth Syst 10(7):1470–1494

Feng Z, Houze RA, Leung LR, Song F, Hardin JC, Wang J, Gustafson WI, Homeyer CR (2019) Spatiotemporal characteristics and large-scale environments of mesoscale convective systems east of the rocky mountains. J Clim. https://doi.org/10.1175/JCLI-D-19-0137.1

Feng Z, Leung LR, Liu N, Wang J, Houze RA, Li J, Hardin JC, Chen D, Guo J (2021) A global high-resolution mesoscale convective system database using satellite-derived cloud tops, surface precipitation, and tracking. J Geophys Res Atmos 126(8):e2020JD034202

Guan P, Chen G, Zeng W, Liu Q (2020) Corridors of Meiyu-season rainfall over Eastern China. J Clim 33(7):2603–2626

Guo Z, Fang J, Sun X, Yang Y, Tang J (2019) Sensitivity of summer precipitation simulation to microphysics parameterization over Eastern China: convection-permitting regional climate simulation. J Geophys Res Atmos 124(16):9183–9204

Guo Z, Fang J, Sun X, Tang J, Yang Y, Tang J (2020) Decadal long convection-permitting regional climate simulations over eastern China: evaluation of diurnal cycle of precipitation. Clim Dyn 54(3):1329–1349

Guo Z, Tang J, Tang J, Wang S, Yang Y, Luo W, Fang J (2022) Object-based evaluation of precipitation systems in convection-permitting regional climate simulation over Eastern China. J Geophys Res Atmos 127(1):e2021JD035645

Haarsma RJ, Roberts MJ, Vidale PL, Senior CA, Bellucci A, Bao Q, Chang P, Corti S, Fučkar NS, Guemas V, von Hardenberg J, Hazeleger W, Kodama C, Koenigk T, Leung LR, Lu J, Luo J-J, Mao J, Mizielinski MS, Mizuta R, Nobre P, Satoh M, Scoccimarro E, Semmler T, Small J, von Storch J-S (2016) High Resolution Model Intercomparison Project (HighResMIP v1.0) for CMIP6. Geosci Model Dev 9(11):4185–4208

Hohenegger C, Kornblueh L, Klocke D, Becker T, Cioni G, Engels JF, Schulzweida U, Stevens B (2020) Climate statistics in global simulations of the atmosphere, from 80 to 2.5 km grid spacing. J Meteorol Soc Jpn Ser II 98(1):73–91

Houze RA (2004) Mesoscale convective systems. Rev Geophys 42(4):RG4003

Houze RA (2018) 100 years of research on mesoscale convective systems. Meteorol Monogr 59:17.11–17.54

Huang D, Zhu J, Zhang Y, Huang A (2013) Uncertainties on the simulated summer precipitation over Eastern China from the CMIP5 models. J Geophys Res Atmos 118(16):9035–9047

Joyce RJ, Janowiak JE, Arkin PA, Xie P (2004) CMORPH: a method that produces global precipitation estimates from passive microwave and infrared data at high spatial and temporal resolution. J Hydrometeorol 5(3):487–503

Kooperman GJ, Pritchard MS, Somerville RCJ (2014) The response of US summer rainfall to quadrupled CO_2 climate change in conventional and superparameterized versions of the NCAR community atmosphere model. J Adv Model Earth Syst 6(3):859–882

Li P, Furtado K, Zhou T, Chen H, Li J, Guo Z, Xiao C (2020a) The diurnal cycle of East Asian summer monsoon precipitation simulated by the Met Office unified model at convection-permitting scales. Clim Dyn 55(1):131–151

Li J, Li Y, Zhao T, Schiemann R, Muetzelfeldt M, Jiang X (2021a) Northeastward propagation of nocturnal precipitation over the Sichuan Basin. Int J Climatol 41(S1):E2863–E2879

Li P, Furtado K, Zhou T, Chen H, Li J (2021b) Convection-permitting modelling improves simulated precipitation over the central and eastern Tibetan Plateau. Q J R Meteorol Soc 147(734):341–362

Li P, Moseley C, Prein AF, Chen H, Li J, Furtado K, Zhou T (2020b) Mesoscale convective system precipitation characteristics over East Asia. Part I: regional differences and seasonal variations. J Clim 33(21):9271–9286

Marsham JH, Dixon NS, Garcia-Carreras L, Lister GMS, Parker DJ, Knippertz P, Birch CE (2013) The role of moist convection in the West African monsoon system: Insights from continental-scale convection-permitting simulations. Geophys Res Lett 40(9):1843–1849

Moseley C, Henneberg O, Haerter JO (2019) A statistical model for isolated convective precipitation events. J Adv Model Earth Syst 11(1):360–375

Moseley C, Berg P, Haerter JO (2013) Probing the precipitation life cycle by iterative rain cell tracking. J Geophys Res Atmos 118(24):13361–13370

Mulcahy JP, Jones C, Sellar A, Johnson B, Boutle IA, Jones A, Andrews T, Rumbold ST, Mollard J, Bellouin N, Johnson CE, Williams KD, Grosvenor DP, McCoy DT (2018) Improved aerosol processes and effective radiative forcing in HadGEM3 and UKESM1. J Adv Model Earth Syst 10(11):2786–2805

Ou T, Chen D, Chen X, Lin C, Yang K, Lai H-W, Zhang F (2020) Simulation of summer precipitation diurnal cycles over the Tibetan Plateau at the gray-zone grid spacing for cumulus parameterization. Clim Dyn 54(7–8):3525–3539

Pearson KJ, Lister GMS, Birch CE, Allan RP, Hogan RJ, Woolnough SJ (2014) Modelling the diurnal cycle of tropical convection across the 'grey zone.' Q J R Meteorol Soc 140(679):491–499

Prein AF, Langhans W, Fosser G, Ferrone A, Ban N, Goergen K, Keller M, Tolle M, Gutjahr O, Feser F, Brisson E, Kollet S, Schmidli J, van Lipzig NP, Leung R (2015) A review on regional convection-permitting climate modeling: demonstrations, prospects, and challenges. Rev Geophys 53(2):323–361

Prein AF, Liu C, Ikeda K, Bullock R, Rasmussen RM, Holland GJ, Clark M (2017a) Simulating North American mesoscale convective systems with a convection-permitting climate model. Clim Dyn 55(1):95–110

Prein AF, Liu C, Ikeda K, Trier SB, Rasmussen RM, Holland GJ, Clark MP (2017b) Increased rainfall volume from future convective storms in the US. Nat Clim Chang 7(12):880–884

Prein AF, Rasmussen R, Stephens G (2017c) Challenges and advances in convection-permitting climate modeling. Bull Am Meteor Soc 98(5):1027–1030

Prein AF, Rasmussen RM, Wang D, Giangrande SE (2021) Sensitivity of organized convective storms to model grid spacing in current and future climates. Philos Trans A Math Phys Eng Sci 379(2195):20190546

Schumacher RS, Rasmussen KL (2020) The formation, character and changing nature of mesoscale convective systems. Nat Rev Earth Environ 1(6):300–314

Song F, Feng Z, Leung LR, Houze RA Jr, Wang J, Hardin J, Homeyer CR (2019) Contrasting spring and summer large-scale environments associated with mesoscale convective systems over the US Great Plains. J Clim 32(20):6749–6767

Song F, Feng Z, Leung LR, Pokharel B, Wang SYS, Chen X, Sakaguchi K, Wang Cc (2021) Crucial roles of eastward propagating environments in the summer MCS initiation over the U.S. great plains. J Geophys Res Atmos 126(16):e2021JD034991

Stevens B, Fiedler S, Kinne S, Peters K, Rast S, Müsse J, Smith SJ, Mauritsen T (2017) MACv2-SP: a parameterization of anthropogenic aerosol optical properties and an associated Twomey effect for use in CMIP6. Geosci Model Dev 10(1):433–452

Stevens B, Satoh M, Auger L, Biercamp J, Bretherton CS, Chen X, Düben P, Judt F, Khairoutdinov M, Klocke D, Kodama C, Kornblueh L, Lin S-J, Neumann P, Putman WM, Röber N, Shibuya R, Vanniere B, Vidale PL, Wedi N, Zhou L (2019) DYAMOND: the DYnamics of the atmospheric general circulation modeled on non-hydrostatic domains. Prog Earth Planet Sci 6(1):1–17

Stevens B, Acquistapace C, Hansen A, Heinze R, Klinger C, Klocke D, Rybka H, Schubotz W, Windmiller J, Adamidis P, Arka I, Barlakas V, Biercamp J, Brueck M, Brune S, Buehler SA, Burkhardt U, Cioni G, Costa-SurÓS M, Crewell S, CrÜGer T, Deneke H, Friederichs P, Henken CC, Hohenegger C, Jacob M, Jakub F, Kalthoff N (2020) The added value of large-eddy and storm-resolving models for simulating clouds and precipitation. J Meteorol Soc Jpn Ser II 98(2):395–435

Taylor CM, Belušić D, Guichard F, Parker DJ, Vischel T, Bock O, Harris PP, Janicot S, Klein C, Panthou G (2017) Frequency of extreme Sahelian storms tripled since 1982 in satellite observations. Nature 544(7651):475

Tomassini L (2018) Mesoscale circulations and organized convection in African Easterly waves. J Atmos Sci 75(12):4357–4381

Vergara-Temprado J, Ban N, Panosetti D, Schlemmer L, Schär C (2020) Climate models permit convection at much coarser resolutions than previously considered. J Clim 33(5):1915–1933

Williams KD, Copsey D, Blockley EW, Bodas-Salcedo A, Calvert D, Comer R, Davis P, Graham T, Hewitt HT, Hill R, Hyder P, Ineson S, Johns TC, Keen AB, Lee RW, Megann A, Milton SF, Rae JGL, Roberts MJ, Scaife AA, Schiemann R, Storkey D, Thorpe L, Watterson IG, Walters DN, West A, Wood RA, Woollings T, Xavier PK (2018) The met office global coupled model 3.0 and 3.1 (GC3.0 and GC3.1) configurations. J Adv Model Earth Syst 10(2):357–380

Yang R, Zhang Y, Sun J, Fu S, Li J (2019) The characteristics and classification of eastward-propagating mesoscale convective systems generated over the second-step terrain in the Yangtze River Valley. Atmos Sci Lett 20(1):e874

Yang R, Zhang Y, Sun J, Li J (2020) The comparison of statistical features and synoptic circulations between the eastward-propagating and quasi-stationary MCSs during the warm season around the second-step terrain along the middle reaches of the Yangtze River. Sci China Earth Sci 63(8):1209–1222

Yang Q, Houze Jr RA, Leung LR, Feng Z (2017) Environments of long-lived mesoscale convective systems over the Central United States in convection permitting climate simulations. J Geophys Res Atmos 122(24):13288–213307

Yu R, Zhou T, Xiong A, Zhu Y, Li J (2007) Diurnal variations of summer precipitation over contiguous China. Geophys Res Lett 34(1):L01704

Yu R, Li J, Chen H, Yuan W (2014) Progress in studies of the precipitation diurnal variation over Contiguous China. J Meteorol Res 28(5):877–902

Yuan J, Houze RA (2010) Global variability of mesoscale convective system anvil structure from A-train satellite data. J Clim 23(21):5864–5888

Yuan W, Yu R, Zhang M, Lin W, Li J, Fu Y (2013) Diurnal cycle of summer precipitation over subtropical East Asia in CAM5. J Clim 26(10):3159–3172

Yun Y, Liu C, Luo Y, Liang X, Huang L, Chen F, Rasmmusen R (2020) Convection-permitting regional climate simulation of warm-season precipitation over Eastern China. Clim Dyn 54(3):1469–1489

Zhang Y, Chen H (2016) Comparing CAM5 and superparameterized CAM5 simulations of summer precipitation characteristics over continental East Asia: mean state, frequency-intensity relationship, diurnal cycle, and influencing factors. J Clim 29(3):1067–1089

Zhang Y, Zhang F, Davis CA, Sun J (2018) Diurnal evolution and structure of long-lived mesoscale convective vortices along the Mei–Yu front over the East China Plains. J Atmos Sci 75(3):1005–1025

Zhou T, Wu B, Wang B (2009) How well do atmospheric general circulation models capture the leading modes of the interannual variability of the Asian-Australian Monsoon? J Clim 22(5):1159–1173

Zhou T, Wu B, Guo Z, He C, Zou L, Chen X, Zhang L, Man W, Li P, Li D, Yao J, Huang X, Zhang W, Zuo M, Lu J, Sun N (2018) A review of East Asian summer monsoon simulation and projection: achievements and problems, opportunities and challenges. Chin J Atmos Sci 42(4):902–934

Zipser EJ, Cecil DJ, Liu C, Nesbitt SW, Yorty DP (2006) Where are the most intense thunderstorms on Earth? Bull Am Meteor Soc 87(8):1057–1072

Publisher's Note Springer Nature remains neutral with regard to jurisdictional claims in published maps and institutional affiliations.